Schaller, M, Vecchia, CD, Schaye, J, Bower, RG, Theuns, T, Crain, RA, Furlong, M and McCarthy, IG

The EAGLE simulations of galaxy formation: the importance of the hydrodynamics scheme

MNRAS 000, 1–16 (2015) Preprint 18 September 2015 Compiled using MNRAS LATEX style file v3.0

The EAGLE simulations of galaxy formation: the importance of the hydrodynamics scheme

Matthieu Schaller[1⋆], Claudio Dalla Vecchia[2,3], Joop Schaye[4], Richard G. Bower[1], Tom Theuns[1], Robert A. Crain[5], Michelle Furlong[1] & Ian G. McCarthy[5]

[1]*Institute for Computational Cosmology, Durham University, South Road, Durham, UK, DH1 3LE*
[2]*Instituto de Astrofísica de Canarias, C/ Vía Láctea s/n, 38205 La Laguna, Tenerife, Spain*
[3]*Departamento de Astrofísica, Universidad de La Laguna, Av. del Astrofísico Franciso Sánchez s/n, 38206 La Laguna, Tenerife, Spain*
[4]*Leiden Observatory, Leiden University, P.O. Box 9513, 2300 RA Leiden, The Netherlands*
[5]*Astrophysics Research Institute, Liverpool John Moores University, 146 Brownlow Hill, Liverpool L3 5RF, UK*

18 September 2015

ABSTRACT

We present results from a subset of simulations from the "Evolution and Assembly of GaLaxies and their Environments" (EAGLE) suite in which the formulation of the hydrodynamics scheme is varied. We compare simulations that use the same subgrid models without recalibration of the parameters but employing the standard GADGET flavour of smoothed particle hydrodynamics (SPH) instead of the more recent state-of-the-art ANARCHY formulation of SPH that was used in the fiducial EAGLE runs. We find that the properties of most galaxies, including their masses and sizes, are not significantly affected by the details of the hydrodynamics solver. However, the star formation rates of the most massive objects are affected by the lack of phase mixing due to spurious surface tension in the simulation using standard SPH. This affects the efficiency with which AGN activity can quench star formation in these galaxies and it also leads to differences in the intragroup medium that affect the X-ray emission from these objects. The differences that can be attributed to the hydrodynamics solver are, however, likely to be less important at lower resolution. We also find that the use of a time step limiter is important for achieving the feedback efficiency required to match observations of the low-mass end of the galaxy stellar mass function.

Key words: cosmology: theory, methods: numerical, galaxies: formation, galaxies: clusters: intracluster medium

1 INTRODUCTION

Cosmological hydrodynamical simulations have started to play a major role in the study of galaxy formation. Recent simulations are able to cover the large dynamical range required to study the large-scale structure dominated by dark matter as well as the centres of halos where baryon physics dominates the evolution. Comparisons of such simulations with observations show broad agreement and help confirm the predictions of the ΛCDM paradigm (e.g. Vogelsberger et al. 2014; Schaye et al. 2015).

Galaxy formation involves a mixture of complex processes and the numerical requirements to simulate all of the relevant scales are enormous. A direct consequence of this is the need to model some of the unresolved processes with subgrid prescriptions. Other processes, taking place on larger scales, can in principle be followed accurately by numerical hydrodynamics solvers. The shocking of cold gas penetrating halos and the turbulence generated by supernova activity within galaxies are examples of the processes that can, in principle, be treated by the hydrodynamics solver. Conversely, the accretion of gas onto black holes and the formation and evolution of stars are examples of processes that occur on scales that are too small to be simulated jointly with the large-scale environment. In practice, however, these two categories of processes are interleaved and it is hence difficult to demonstrate convergence even of the purely hydrodynamical processes. Practitioners are therefore forced to chose a numerical hydrodynamics solver that gives accurate results at the resolution of interest.

Many numerical techniques (e.g. Adaptive Mesh Refinement, particle techniques, moving-mesh techniques, mesh-free techniques) have been developed over the years to solve the equations of hydrodynamics, each of them coming in different "flavours", i.e. coming with slightly different equations, assumptions and limitations. For the processes that can be simulated using standard numerical solvers, the main question is how the various parameters that enter these hydrodynamics solvers affect the formation of galaxies in the simulations. For example, it has been reported that different numerical techniques and choices of parameters affect the disruption of a cold gas blob in a low-density hot medium, a case di-

⋆ E-mail: matthieu.schaller@durham.ac.uk

rectly relevant the accretion of gas and satellite of galaxies (Frenk et al. 1999; Marri & White 2003; Okamoto et al. 2003; O'Shea et al. 2005; Agertz et al. 2007; Wadsley et al. 2008; Mitchell et al. 2009; Kereš et al. 2012; Sijacki et al. 2012). In principle, the values of these numerical parameters can be set by performing controlled numerical experiments for which the solution is known.

In the case of simulations using Smoothed Particle Hydrodynamics (SPH) solvers (Lucy 1977; Gingold & Monaghan 1977) (see Springel 2010a; Price 2012, for reviews), the free parameters relate to the treatment of shocks, artificial viscosity and conduction and are related to the way the SPH equations are derived, leading to different flavours of the technique. Performing controlled tests such as Sedov explosions or Kelvin-Helmoltz instabilities (e.g. Price 2008; Read et al. 2010; Springel 2010b; Hu et al. 2014; Hopkins 2015; Beck et al. 2015) enables the simulator to identify well-motivated values for the parameters and understand the limitations of the formulation. Early flavours of SPH had issues dealing with discontinuities in the fluid. One of many examples of this problem is the "blob test" of Agertz et al. (2007) which was widely used in the literature to demonstrate the failure of SPH. A lot of effort has then been spent by the community to improve the situation and many alternative solutions have been proposed to overcome the appearance of spurious surface tension that prevents the correct mixing of phases. Solutions using either an alternative formulation of the equations in which the discontinuities are smoothed were proposed (e.g. Ritchie & Thomas 2001; Read et al. 2010; Abel 2011; Saitoh & Makino 2013) as well as solution involving additional terms diffusing material across the discontinuities (e.g. Price 2008). Both types of solutions to the discontinuity problem present shortcomings (see discussion at the end of Section 2.2) and this motivated the implementation of SPH used in this paper, which uses a combination of both solutions. Although one can in principle calibrate the free parameters using tests, it is unclear whether there is a single set of values that is suitable for all problems and whether these parameter values are also the best choice when performing simulations of very hot and diffuse conditions, such as those present in the hot haloes of galaxies (e.g. Sembolini et al. 2015). Moreover, the large gap in resolution between these controlled experiments and cosmological simulations makes the extrapolation of the solver's behaviour a difficult and uncertain task. The correct treatment of entropy jumps across shocks or of the spurious viscosity that can appear in differentially rotating disks can have direct consequences for the population of simulated galaxies.

In their comprehensive study of galaxy formation models, Scannapieco et al. (2012) used multiple hydrodynamics solvers coupled to multiple sets of subgrid models to simulate the formation of galaxies in a single halo and to study the relative impact of the choice of solver and subgrid model. One of their main findings was that the variations in the hydrodynamics solvers led to much smaller changes in the final results than did the changes to the subgrid model parameters. This was especially the case for the prescription of feedback, which can change the final galaxy tremendously (e.g. Schaye et al. 2010; Haas et al. 2013; Vogelsberger et al. 2013; Crain et al. 2015). A more controlled experiment was performed by Kereš et al. (2012), who compared two hydrodynamics solvers but used only a simplified model of galaxy formation and, apart for the most massive galaxies, found very little difference in the galaxy population despite the large gap in accuracy between the hydro solvers tested. Their two simulations, however, displayed significant differences in the gas properties, especially in the cold gas fractions. More realistic subgrid models, especially of feedback, are likely to suppress some of these difference.

Building on those studies, we attempt to quantify the impact of the uncertainties in two different implementations of SPH solvers on a simulated galaxy population. The EAGLE simulation project (Schaye et al. 2015; Crain et al. 2015) uses a state-of-the-art implementation of SPH, called ANARCHY (Dalla Vecchia in prep., see also appendix A of Schaye et al. 2015) and the time-step limiter of Durier & Dalla Vecchia (2012). EAGLE's subgrid model parameters were calibrated to reproduce the observed local Universe population of galaxies. In this study, we vary the hydrodynamics solver. We compare ANARCHY to the older Springel & Hernquist (2002) flavour of SPH implemented in the GADGET code (Springel 2005) and compare the resulting galaxy population to the one in the reference EAGLE simulation and to those in simulations with weaker/stronger stellar feedback and to runs without AGN feedback. Since EAGLE broadly reproduces the observed galaxy population, our test is especially relevant and enables us to disentangle the effects of the hydro solver from the effects of the subgrid model.

This paper is structured as follows. In section 2 the EAGLE model and the two flavours of SPH that we consider are described. Section 3 discusses the impact of the hydrodynamics solver on the simulated galaxies whilst Section 4 presents differences in the gas properties of the haloes. A summary of our findings can be found in Section 5.

Throughout this paper, we assume a *Planck2013* flat ΛCDM cosmology (Planck Collaboration et al. 2014) ($h = 0.6777$, $\Omega_b = 0.04825$, $\Omega_m = 0.307$ and $\sigma_8 = 0.8288$) and express all quantities without h factors.

2 THE EAGLE SIMULATIONS

The EAGLE set consists of a series of cosmological simulations with state-of-the-art subgrid models and smoothed particle hydrodynamics. The simulations have been calibrated to reproduce the observed galaxy stellar mass function, the relation between galaxy stellar mass and supermassive black hole mass and galaxy mass-size relation at $z = 0.1$. The simulations also broadly reproduce a large variety of other observables such as the Tully-Fisher relation and specific star formation rates (Schaye et al. 2015), the H_2 and H I properties of galaxies (Lagos et al. 2015, Bahe et al. submitted), the evolution of the galaxy stellar mass function (Furlong et al. 2015), the column density distribution of intergalactic metals (Schaye et al. 2015) and H I (Rahmati et al. 2015) as well as galaxy rotation curves (Schaller et al. 2015) and luminosities (Trayford et al. 2015).

The EAGLE simulations discussed in this paper follow $752^3 \approx 4.3 \times 10^8$ dark matter particles and the same number of gas particles in a 50^3 Mpc^3 cubic volume from ΛCDM initial conditions. Note that the simulation volumes considered here are a factor of eight smaller than the main 100^3 Mpc^3 EAGLE run. The mass of a dark matter particle is $m_{\rm DM} = 9.7 \times 10^6$ M$_\odot$ and the initial mass of a gas particle is $m_{\rm g} = 1.8 \times 10^6$ M$_\odot$. The gravitational softening length is 700 pc (Plummer equivalent) in physical units below $z = 2.8$ and 2.66 kpc (comoving) at higher redshifts. The simulations were run with a heavily modified version of the GADGET-3 N-body tree-PM and SPH code, last described in Springel (2005). The changes include the introduction of the subgrid models described in the next subsection as well as the implementation of the ANARCHY flavour of SPH, whose impact on the simulation outcome is the topic of this paper. In the next subsections we will describe the subgrid model used in the EAGLE simulations with a special emphasis on those aspects of the model that are directly

impacted upon by the hydrodynamic scheme. For the sake of completeness, we then briefly describe both the standard GADGET and ANARCHY flavours of SPH.

2.1 Subgrid models and halo identification

Radiative cooling is implemented using element-by-element rates (Wiersma et al. 2009a) for the 11 most important metals in the presence of the CMB and UV/X-ray backgrounds given by Haardt & Madau (2001). To prevent artificial fragmentation, the cold and dense gas is not allowed to cool to temperatures below those corresponding to an equation of state $P_{\rm eos} \propto \rho^{4/3}$ that is designed to keep the Jeans mass marginally resolved (Schaye & Dalla Vecchia 2008). Star formation is implemented using a pressure-dependent prescription that reproduces the observed Kennicutt-Schmidt star formation law (Schaye & Dalla Vecchia 2008) and uses a threshold that captures the metallicity dependence of the transition from the warm, atomic to the cold, molecular gas phase (Schaye 2004). Star particles are treated as single stellar populations with a Chabrier (2003) IMF evolving along the tracks provided by Portinari et al. (1998). Metals from supernovae and AGB stars are injected into the interstellar medium (ISM) following the model of Wiersma et al. (2009b) and stellar feedback is implemented by the stochastic injection of thermal energy into the gas as described in Dalla Vecchia & Schaye (2012). The amount of energy injected into the ISM per feedback event depends on the local gas metallicity and density in an attempt to take into account the unresolved structure of the ISM (Schaye et al. 2015; Crain et al. 2015). Supermassive black hole seeds are injected in halos above $10^{10}h^{-1}{\rm M}_{\odot}$ and grow through mergers and accretion of low angular momentum gas (Rosas-Guevara et al. 2013; Schaye et al. 2015). AGN feedback is performed by injecting thermal energy into the gas directly surrounding the black hole (Booth & Schaye 2009; Dalla Vecchia & Schaye 2012).

The subgrid model was calibrated (by adjusting the intensity of stellar feedback and the accretion rate onto black holes) so as to reproduce the present-day galaxy stellar mass function and galaxy sizes (Schaye et al. 2015). As discussed by Crain et al. (2015), this latter requirement is crucial to obtain a galaxy population that evolves with redshift in a similar fashion to the observed populations (Furlong et al. 2015).

Haloes were identified using the Friends-of-Friends (FoF) algorithm (Davis et al. 1985) with linking length 0.2 times the mean interparticle distance, and bound structures within them were then identified using the SUBFIND code (Springel et al. 2001; Dolag et al. 2009). A sphere centred at the minimum of the gravitational potential of each subhalo is grown until the mass contained within a given radius, R_{200}, reaches $M_{200} = 200\left(4\pi\rho_{\rm cr}(z)R_{200}^3/3\right)$, where $\rho_{\rm cr}(z) = 3H(z)^2/8\pi G$ is the critical density at the redshift of interest.

2.2 SPH implementations

All simulations that are compared in this study use modifications of the Gadget-3 code. We use both the default flavour of SPH documented in Springel (2005) and the more recent flavour nicknamed ANARCHY (Dalla Vecchia (in prep.), see also appendix A of Schaye et al. 2015) implemented as a modification to the default code. For completeness, we describe both sets of hydrodynamical equations in this section without derivations. For comprehensive descriptions and motivations, see the review by Price (2012) and the description of the alternative formalism by Hopkins (2013, 2015). A formulation of SPH that is similar to ANARCHY is presented in Hu et al. (2014). Note that apart from the differences highlighted in this section, the codes (and parameters) used for both types of simulations are identical.

2.2.1 *Default* GADGET-2 *SPH*

In its default version, GADGET-2 uses the fully conservative SPH equations introduced by Springel & Hernquist (2002). We will label this "GADGET SPH" in the remainder of this paper and restrict our discussion of the model to the 3D case. As in any flavour of SPH, the starting point is a the choice of a smoothing function to reconstruct field quantities at any point in space from a weighted average over the surrounding particles. In the case of gas density, at position $\mathbf{x}_i$. the equation reads

$$\rho_i = \sum_j m_j W\left(|\mathbf{x}_i - \mathbf{x}_j|, h_i\right), \tag{1}$$

where $W(|\mathbf{r}|, h)$ is the spherically symmetric kernel function. In the case of GADGET, the M_4 cubic B-spline function is used and reads

$$W(r,h) = \frac{8}{\pi h^3}\begin{cases} 1-6\left(\frac{r}{h}\right)^2+6\left(\frac{r}{h}\right)^3 & \text{if} \quad 0 \leqslant r \leqslant \frac{h}{2} \\ 2\left(1-\frac{r}{h}\right)^3 & \text{if} \quad \frac{h}{2} < r \leqslant h \\ 0 & \text{if} \quad r > h. \end{cases}$$

The smoothing length h_i of a particle is obtained by requiring that the weighted number of neighbours

$$N_{\rm ngb} = \frac{4}{3}\pi h_i^3 \sum_j W\left(|\mathbf{x}_i - \mathbf{x}_j|, h_i\right) \tag{2}$$

of the particle is close to a pre-defined constant; $N_{\rm ngb} = 48$ in our case. Note, however, that contrary to what is often written in the literature, GADGET defines the smoothing length as the cut-off radius of the kernel and not as the more physical FWHM of the kernel function (Dehnen & Aly 2012).

The quantity integrated in time alongside the velocities and positions of the particles is the entropic function[1] $A_i = P_i/\rho_i^{\gamma}$, defined in terms of the pressure P_i and polytropic index γ. The equations of motion are then given by

$$\frac{{\rm d}\mathbf{v}_{\rm i}}{{\rm dt}} = -\sum_j m_j\left[\frac{P_i}{\Omega_i\rho_i^2}\nabla_i W_{ij}(h_i) + \frac{P_j}{\Omega_j\rho_j^2}\nabla_i W_{ij}(h_j)\right], \tag{3}$$

where Ω_i accounts for the gradient of the smoothing length,

$$\Omega_i = 1 + \frac{h_i}{3\rho_i}\sum_j m_j \frac{\partial W_{ij}(h_i)}{\partial h} \tag{4}$$

and $W_{ij}(h_i) \equiv W(\mathbf{x}_i - \mathbf{x}_j, h_i)$. In the absence of radiative cooling or thermal diffusion terms, the entropic function of each particle is a constant in time. Only radiative cooling, feedback events (see the previous section) and shocks will change the entropic function.

In order to capture shocks, artificial viscosity is implemented by adding a term to the equations of motion (eq. 3) to evolve the entropic function accordingly:

[1] This quantity is not the thermodynamic entropy s but a monotonic function of it.

$$\frac{\mathrm{d}\mathbf{v}_\mathrm{i}}{\mathrm{dt}} \overset{\text{visc.}}{=} -\frac{1}{4}\sum_j m_j \Pi_{ij} \nabla \overline{W}_{ij} \left(f_i + f_j\right)$$

$$\frac{\mathrm{dA}_\mathrm{i}}{\mathrm{dt}} \overset{\text{visc.}}{=} \frac{1}{8}\frac{\gamma-1}{\rho_i^{\gamma-1}}\sum_j m_j \Pi_{ij} \left(\mathbf{v}_i - \mathbf{v}_j\right)\cdot \nabla \overline{W}_{ij} \left(f_i + f_j\right),$$

with $\overline{W}_{ij} \equiv (W_{ij}(h_i) + W_{ij}(h_j))$ and the viscous tensor (Π_{ij}) and shear flow switch f_i defined below. Following Monaghan (1997), the viscous tensor, which plays the role of an additional pressure in the equations of motion, is defined in terms of the particle's sound speed, $c_i = \sqrt{\gamma P_i/\rho_i}$, as

$$\Pi_{ij} = -\alpha \frac{(c_i + c_j - 3w_{ij})\, w_{ij}}{\rho_i + \rho_j}, \tag{5}$$

$$w_{ij} = \min\left(0, \frac{(\mathbf{v}_j - \mathbf{v}_i)\cdot(\mathbf{x}_i - \mathbf{x}_j)}{|\mathbf{x}_i - \mathbf{x}_j|}\right) \tag{6}$$

with the dimensionless viscosity parameter set to the commonly used value of $\alpha = 2$ in our simulations. Finally, to prevent the application of viscosity in the case of pure shear flows, the switch proposed by Balsara (1995) is used:

$$f_i = \frac{|\nabla\cdot\mathbf{v}_i|}{|\nabla\cdot\mathbf{v}_i| + |\nabla\times\mathbf{v}_i| + 10^{-4}c_i/h_i}, \tag{7}$$

with the last term in the denominator added to avoid numerical instabilities. The divergence and curl of the velocity field are computed in the standard SPH way (e.g. Price 2012).

2.2.2 ANARCHY *SPH*

The first change in ANARCHY with respect to GADGET is the choice of kernel function. More accurate estimators for both the field quantities and their derivatives can be obtained by using Wendland (1995) kernels (Dehnen & Aly 2012). ANARCHY uses the C_2 kernel. This kernel function is not affected by the pairing instability, which occurs when high values of N_ngb are used with spline kernels. It reads

$$W(r,h) = \frac{21}{2\pi h^3}\begin{cases} \left(1-\frac{r}{h}\right)^4\left(1+4\frac{r}{h}\right) & \text{if} \quad 0\leqslant r\leqslant h \\ 0 & \text{if} \quad r > h. \end{cases}$$

To keep the effective resolution of the simulation similar between the two flavours of SPH, we use $N_\mathrm{ngb} = 58$ with this kernel. This yields the same kernel FWHM as obtained for the cubic kernel[2] with $N_\mathrm{ngb} = 48$. Note, however, that the C_2 kernel only exhibits better behaviour than the cubic spline kernel when large numbers of neighbours ($N_\mathrm{ngb} \gtrsim 100$) are used (Dehnen & Aly 2012). We use the C_2 kernel with $N_\mathrm{ngb} = 58$ to be consistent with both the EAGLE resolution and the hydrodynamics studies of Dalla Vecchia (in prep.) who used the same kernel but more neighbours.

The equations of motion used in the ANARCHY flavour of SPH are based on the Pressure-Entropy formulation of Hopkins (2013), a generalisation of the earlier solutions of Ritchie & Thomas (2001), Read et al. (2010), Abel (2011) and Saitoh & Makino (2013). The two quantities carried by particles that are integrated forward in time are again the velocity and the entropic function. Alongside the density, which is computed in the usual way (Eq. 1), two additional smoothed quantities are introduced in this formulation of SPH: the weighted density

$$\bar{\rho}_i = \frac{1}{A_i^{1/\gamma}}\sum_j m_j A_j^{1/\gamma} W\left(|\mathbf{x}_i - \mathbf{x}_j|, h_i\right) \tag{8}$$

and its associated weighted pressure, $\bar{P}_i = A_i\bar{\rho}_i^\gamma$. Despite having the same units as the regular density, its weighted counterpart should only be understood as an intermediate quantity entering other equations and should not be used as the gas density. Using these two new quantities, the equation of motion for the particle velocities becomes

$$\frac{\mathrm{d}\mathbf{v}_\mathrm{i}}{\mathrm{dt}} = -\sum_j m_j \left[\frac{A_j^{1/\gamma}}{A_i^{1/\gamma}}\frac{\bar{P}_i}{\bar{\rho}_i^2}\Omega_{ij}\nabla_i W_{ij}(h_i) + \frac{A_i^{1/\gamma}}{A_j^{1/\gamma}}\frac{\bar{P}_j}{\bar{\rho}_j^2}\Omega_{ji}\nabla_j W_{ij}(h_j)\right] \tag{9}$$

with the terms accounting for the gradients in the smoothing length reading

$$\Omega_{ij} = 1 - \frac{1}{A_i^{1/\gamma}}\left(\frac{h_i}{3\rho_i}\frac{\partial \bar{P}_i^{1/\gamma}}{\partial h_i}\right)\left(1 + \frac{h_i}{3\rho_i}\right)^{-1}. \tag{10}$$

The use of the smoothed quantities $\bar{P}_i$ and $\bar{\rho}_i$ in the equations of motion smooths out the spurious pressure jumps appearing at contact discontinuities in older formulations of SPH (Saitoh & Makino 2013; Hopkins 2013).

As in all versions of SPH, artificial viscosity has to be added to capture shocks. In the ANARCHY formulation of SPH, this is done following the method of Cullen & Dehnen (2010). Their scheme is the latest iteration of a series of improvements to the standard (Monaghan 1997) viscosity term that started with the proposal of Morris & Monaghan (1997) to assign individual viscosities α_i to each particle. Improving on the work of Rosswog et al. (2000), Price (2004) and Wetzstein et al. (2009), Cullen & Dehnen (2010) proposed a differential equation for α_i that is solved alongside the equations of motion (Eqn. 9):

$$\dot{\alpha}_i = 2lv_{\mathrm{sig},i}\left(\alpha_{\mathrm{loc},i} - \alpha_i\right)/h_i, \tag{11}$$

with $l = 0.01$ and the signal velocity $v_{\mathrm{sig},i}$ introduced below. The local viscosity estimator $\alpha_{\mathrm{loc},i}$ is given by

$$\alpha_{\mathrm{loc},i} = \alpha_{\max}\frac{h_i^2 S_i}{v_{\mathrm{sig},i}^2 + h_i^2 S_i}, \tag{12}$$

where $\alpha_{\max} = 2$ and $S_i = \max\left(0, -\frac{d}{dt}\left(\nabla\cdot\mathbf{v}_i\right)\right)$ is the shock detector. After passing through a shock, $S_i = 0$ and hence $\alpha_{\mathrm{loc},i} = 0$, leading to a decrease in α_i. We impose $\alpha_i > \alpha_{\min} = 0.05$ to facilitate particle re-ordering. The signal velocity is constructed to capture the maximum velocity at which information can be transferred between particles whilst remaining positive:

$$v_{\mathrm{sig},i} = \max_{|\mathbf{x}_{ij}|\leqslant h_i}\left(\frac{1}{2}\left(c_i + c_j\right) - \min(0, \mathbf{v}_{ij}\cdot\hat{\mathbf{x}}_{ij})\right), \tag{13}$$

with $\hat{\mathbf{x}}_{ij} = (\mathbf{x}_i - \mathbf{x}_j)/|\mathbf{x}_i - \mathbf{x}_j|$ and $\mathbf{v}_{ij} = \mathbf{v}_j - \mathbf{v}_i$.

The individual viscosity coefficients α_i are then combined to

[2] Expressing our resolution in terms of the local inter-particle separation (Price 2012; Dehnen & Aly 2012) gives $\eta = \mathrm{FWHM}(W(r,h))/\Delta x = 1.235$ for both kernels.

enter the equations of motion in a similar way as in the GADGET formulation. Equations 5 and 6 are replaced by:

$$\Pi_{ij} = -\frac{\alpha_i + \alpha_j}{2}\frac{(c_i + c_j - 3w_{ij})\,w_{ij}}{\rho_i + \rho_j}, \quad (14)$$

$$w_{ij} = \min\left(0, \frac{(\mathbf{v}_j - \mathbf{v}_i)\cdot(\mathbf{x}_i - \mathbf{x}_j)}{|\mathbf{x}_i - \mathbf{x}_j|}\right). \quad (15)$$

Note that contrary to Hu et al. (2014), we do not implement expensive matrix calculations (Cullen & Dehnen 2010) for the calculation of the velocity divergence time derivative entering the shock detector S_i as we found that using the standard SPH expressions was sufficient for the accuracy we targeted.

The last improvement included in the ANARCHY flavour of SPH is the use of some entropy diffusion between particles. SPH is by construction non-diffusive (e.g. Price 2012) and does, hence, not incorporate the thermal conduction that may be required to faithfully reproduce the micro-scale mixing of gas phases. We implement a small level of numerical diffusion following the recipe of Monaghan (1997) and Price (2008). We compute the internal energies from the entropies and these are then used in the equations for the diffusion. The use of the pressure-entropy formalism (eq. 9) prevents the formation of spurious surface tension at contact discontinuities (Hopkins 2013). This small amount of numerical diffusion allows the particles to mix their entropies at the discontinuity and hence create one single phase (Dalla Vecchia in prep.). The diffusion is hence used to solve a numerical problem and not to introduce a macroscopic conduction. This results in cluster entropy profiles in agreement with the results from grid and moving-mesh codes (see the comparison of Sembolini et al. 2015, which includes ANARCHY). We compute the rate of change of the conduction using the second derivative of the energy. This means that large conduction values $\alpha_{\rm diff}$ are triggered by discontinuities in the first derivative of the energy, not by smooth pressure gradients as in (self-)gravitating objects. Moreover, $\alpha_{\rm diff}$ may take some time to increase while the smoothing of the discontinuity decreases its rate. Finally, our rate is lowered to only a few percent of the computed value for the value of the free parameter β employed, contrary to almost all the implementations in the literature. This largely reduces spurious pressure waves. More specifically, the equation describing the evolution of the entropy includes a new term,

$$\frac{{\rm dA_i}}{{\rm dt}} \stackrel{\rm diff.}{=} \frac{1}{\bar{\rho}^{\gamma-1}}\sum_j \alpha_{{\rm diff},ij} v_{{\rm diff},ij}\frac{m_j}{\rho_i+\rho_j}\left(\frac{\bar{P}_i}{\bar{\rho}_i} - \frac{\bar{P}_j}{\bar{\rho}_j}\right)\overline{W}_{ij}, \quad (16)$$

with the diffusion velocity given by $v_{{\rm diff},ij} = \max(c_i + c_j + (\mathbf{v}_i - \mathbf{v}_j)\cdot(\mathbf{x}_i - \mathbf{x}_j)\,/\,|\mathbf{x}_i - \mathbf{x}_j|, 0)$ and the diffusion coefficient by $\alpha_{{\rm diff},ij} = \frac{1}{2}(\alpha_{{\rm diff},i} + \alpha_{{\rm diff},j})$. The individual diffusion coefficients are evolved alongside the other thermodynamic variables following the differential equation

$$\dot{\alpha}_{{\rm diff},i} = \beta\frac{h_i\nabla_i^2\left(\bar{P}_i/(\gamma-1)\bar{\rho}_i\right)}{\sqrt{\bar{P}_i/(\gamma-1)\bar{\rho}_i}}, \quad (17)$$

where, as discussed above, we adopt $\beta = 0.01$. We further impose $0 < \alpha_{{\rm diff},i} < 1$, but note that the upper limit is rarely reached, even for large discontinuities.

2.3 Thermal energy injection and time-step limiter

A crucial aspect of the stellar feedback implementation used in EAGLE and described in Dalla Vecchia & Schaye (2012), is the instantaneous injection of large amounts of thermal energy Δu in the ISM. This injection is performed by raising the temperature of a gas particle by $\Delta T = 10^{7.5}$ K, a value much larger than the average temperature of the warm ISM. In the GADGET formulation of SPH, this is implemented by changing the entropy A_i of a particle. In the case of ANARCHY, the situation is more complex since the densities themselves are weighted by the entropies, which implies that a change in the entropy will affect both quantities entering the equations of motion of all the particles in a given neighbourhood. Hence, changing the internal entropy of just one single particle will *not* lead to the correct change of energy (across all particles in the simulation volume) of the gas. The thermal energy injected in the gas will be different (typically lower) from what is expected by a simple rise in A_i, leading to a seemingly inefficient feedback event.

This problem is alleviated in the EAGLE code by the use of a series of iterations during which the values of A_i and ρ_i are changed until they have converged to values for which the total energy injection is close to the imposed value:

$$A_{i,n+1} = \frac{(\gamma-1)(u_{\rm old} + \Delta u)}{\bar{\rho}_{i,n}^{\gamma-1}},$$

$$\bar{\rho}_{i,n+1} = \frac{\bar{\rho}_{i,n}A_n^{1/\gamma} - m_i W(0,h_i)A_{i,n}^{1/\gamma} + m_i W(0,h_i)A_{i,n+1}^{1/\gamma}}{A_{i,n+1}^{1/\gamma}}.$$

This approximation is only valid for reasonable values of Δu and only leads to the injection of the correct amount of energy if the energy is injected into one particle in a given neighbourhood, as is the case in most stellar feedback events. This scheme typically leads to converged values (at better than the 5% level) in one or two iterations. When large amounts of energy are injected into multiple neighbouring particles, as can happen in some AGN feedback events, this approximation is not sufficient to properly conserve energy (across all particles in a given kernel neighbourhood). To avoid this, we limit the number of particles being heated at the same time to 30% of the AGN's neighbours. If this threshold is exceeded, the time step of the BH is decreased and the remaining energy is kept for injection at the next time step. Isolated explosion tests have shown that this limit leads to the correct amount of energy being distributed.

As was pointed out by Saitoh & Makino (2009), the conservation of energy in SPH following the injection of large amounts of energy requires the reduction of the integration time-step of the particles receiving energy as well as those of its direct neighbours. This was further refined by Durier & Dalla Vecchia (2012), who demonstrated that energy conservation can only be achieved if the time-step of the particles is updated according to their new hydrodynamical state. This latter time-step limiter is applied in both the GADGET-SPH and ANARCHY-SPH simulations used in sections 3 and 4 of this paper. We discuss its influence on galaxy properties in subsections 3.1 and 3.2.

3 GALAXY POPULATION AND EVOLUTION THROUGH COSMIC TIME

As discussed by Schaye et al. (2015) and Crain et al. (2015), the subgrid models of stellar and AGN feedback are only an incomplete representation of the physical processes taking place in the unresolved multiphase ISM. In particular, because radiative losses and momentum cancellation associated with feedback from star formation and AGN in the multiphase ISM cannot be predicted

from first principles, the simulations cannot make ab initio predictions for the stellar and black hole masses. In a fashion similar to the semi-analytic models, the subgrid models for feedback in the EAGLE simulations have therefore been calibrated to reproduce the $z = 0.1$ galaxy stellar mass function and the relations between galaxy size and mass and between the mass of the central supermassive black hole and the galaxy. The details of this calibration procedure are described in Crain et al. (2015). In this section, we will present the basic properties of our simulated galaxy population when the hydrodynamic scheme is reverted to the commonly used GADGET-SPH formalism. We will specifically focus on the galaxy stellar mass function and galaxy sizes before turning towards the star formation rates.

We stress that the model parameters have not been recalibrated when switching our hydrodynamics scheme back to GADGET-SPH.

3.1 The galaxy stellar mass function

In Fig. 1, we show the galaxy stellar mass function (GSMF) at $z = 0.1$ computed in spherical apertures of 30 kpc around the centre of potential of the haloes. As discussed by Schaye et al. (2015), this choice of aperture gives a simple way to distinguish the galaxy and the ICL. The blue and red lines correspond to our simulations with the ANARCHY and GADGET flavours of SPH, respectively. We use dashed lines when fewer than 10 objects populate a (0.2 dex) stellar mass bin and dotted lines when the galaxy mass drops below our resolution limit (for resolution considerations, see Schaye et al. 2015). The two hydrodynamic schemes lead to very similar GSMFs with significant differences only appearing at $M_* > 2 \times 10^{11}$ M$_\odot$, where the small number of objects in the volume prevents a strong interpretation of the deviation, based solely on that diagnostic. The white circles and grey squares correspond to the observationally inferred GSMFs from the GAMA (Li & White 2009) and SDSS (Baldry et al. 2012) surveys, respectively. The two simulated galaxy populations undershoot the break of the stellar mass function by a similar amount and are in a similarly good agreement ($\lesssim 0.2$ dex) with the data. The choice of hydrodynamic solver seems to only impact the mass and abundance of the most massive galaxies in our cosmological simulations. We re-iterate that there has been no recalibration of the subgrid parameters between the GADGET and ANARCHY simulations.

In order to compare the contribution of hydrodynamics uncertainties to the uncertainties arising from the subgrid models, we show using green and yellow lines two additional models using the ANARCHY flavour of SPH but with feedback from star formation injecting half and twice as much energy, respectively. These simulations are the models WeakFB and StrongFB introduced by Crain et al. (2015) and reduced or increased the number of feedback events taking place, whilst keeping the amount of energy injected per event constant. They have been run in smaller volumes (25^3 Mpc^3), leading to poorer statistics at the high-mass end. These changes in the amount of energy injected in the ISM lead to much larger differences in the GSMF than changing the flavour of SPH used for the simulation.

The large impact of variations of the subgrid model for stellar feedback on the simulated population and on single galaxies can also be appreciated from the large range of outcomes of the different models in the OWLS suite (Schaye et al. 2010; Haas et al. 2013) and AQUILA projects (Scannapieco et al. 2012). Our work, however, uses a higher resolution than was accessible in the OWLS suite for $z = 0$ and contrary to AQUILA uses a cosmological volume and can hence study the effect of the hydrodynamics

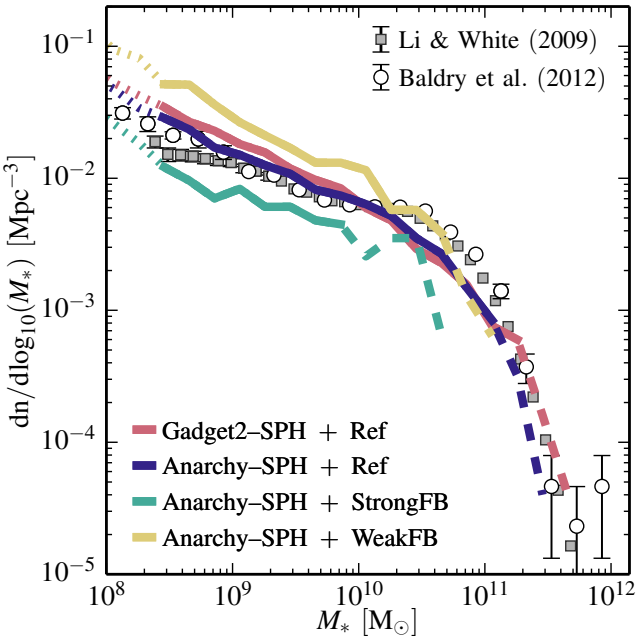

Figure 1. The $z = 0.1$ GSMF of the L050N0752 simulations using ANARCHY SPH (blue line, the EAGLE default) and GADGET SPH (red line). Curves are drawn with dotted lines where galaxies are comprised of fewer than 100 star particles, and dashed lines where the GSMF is sampled by fewer than 10 galaxies per 0.2 dex mass bin. Data points show measurements with 1σ error bars from the SDSS (Li & White 2009, filled squares), and GAMA (Baldry et al. 2012, open circles) surveys. The yellow and green lines show the GSMF of the L025N0376 simulations with twice weaker and twice stronger feedback from star formation respectively, in a smaller 25^3 Mpc^3 volume. The differences due to the choice of hydrodynamics scheme are smaller than the differences due to uncertainties in the sub-grid modelling.

scheme from dwarf galaxies to group-sized haloes. The study of Kereš et al. (2012), which compared the AREPO (Springel 2010b) and GADGET-SPH hydro solvers but using simple subgrid models, came to the same conclusion: the choice of hydrodynamics scheme has little impact on the stellar mass function of simulated galaxies at intermediate mass, only the most massive objects are affected. Interestingly, the differences they observed in high mass galaxies are exactly opposite to our findings: the more accurate solver (in their case AREPO) produces more massive galaxies than the simulation using GADGET-SPH. This confirms that the source terms arising from the physical modelling of the unresolved processes in the ISM, especially the modelling of AGN feedback (see the discussion below in Section 4.2), clearly dominate the uncertainty budget.

We now turn to the impact of the time-step limiter on the simulated galaxy population. As was demonstrated by Durier & Dalla Vecchia (2012), the absence of a time-step limiter leads to the non-conservation of energy during feedback events. The energy of the system after the injection is larger than expected. This implies that a simulation without time-step limiter will have a spuriously high feedback efficiency. In order to test this, we ran a simulation in a 25^3 Mpc^3 volume using the Ref subgrid model and the ANARCHY-SPH scheme but with the Durier & Dalla Vecchia (2012) time-step limiter switched off. Since this simulation volume is too small to be representative, it is more informative to study the relation between halo mass and stellar mass.

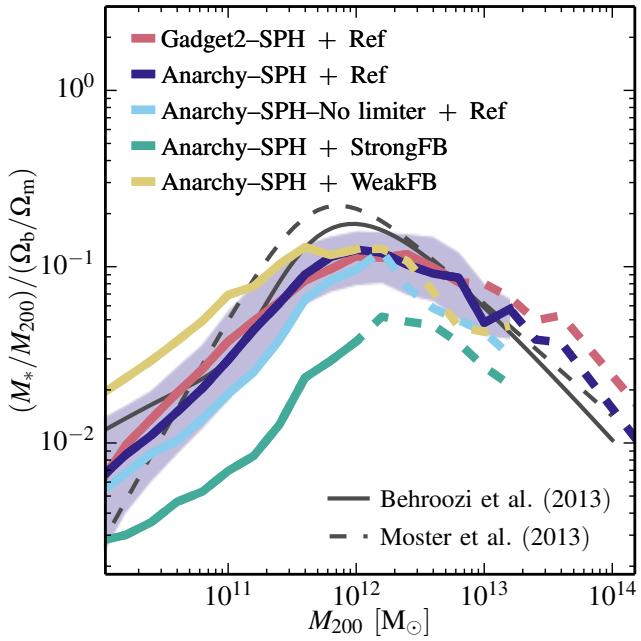

Figure 2. The median ratio of the stellar and halo mass of central galaxies, as a function of halo mass M_{200} and normalised by the cosmic baryon fraction at $z = 0.1$ for both the L050N0752 ANARCHY SPH (blue line) and GADGET SPH (red line) simulations. Curves are drawn with dashed lines where the GSMF is sampled by fewer than 10 galaxies per bin. The 1σ scatter about the median of the ANARCHY run is denoted by the blue shaded region. The solid and dashed grey lines show the multi-epoch abundance matching results of Behroozi et al. (2013) and Moster et al. (2013) respectively. The yellow and green lines show the GSMF of the L025N0376 simulations with twice weaker and twice stronger feedback from star formation respectively. The cyan line corresponds to the simulation using the ANARCHY formulation of SPH and the reference subgrid model, but without the time-step limiter. The absence of the time-step limiter artificially increases the efficiency of the feedback and has a greater impact than the choice of hydro solver.

In Fig. 2, we therefore show the relation between halo mass (M_{200}) and galaxy formation efficiency (M_*/M_{200}) for central galaxies at $z = 0.1$. As for all other figures, the blue and red lines correspond to the ANARCHY-SPH and GADGET-SPH simulations respectively, both using the time-step limiter. We show the simulation using twice stronger and twice weaker feedback with green and yellow lines respectively. These are the same simulations that were shown in Fig. 1. The stronger feedback from star formation leads to a lower stellar mass formed in a given halo than in the Ref model, as was discussed by Crain et al. (2015). As expected from the GSMF, galaxy formation efficiency is strongly moderated by the feedback parameters. Finally, we show in cyan the simulation using the Ref subgrid model but without the time-step limiter. This simulation displays a lower stellar mass in a given halo than its counterpart using the limiter. This indicates that the feedback was indeed more efficient at quenching star formation in that simulation, as expected from the analysis of Durier & Dalla Vecchia (2012). This is a purely numerical effect that has to be corrected by the use of small time-steps in regions where feedback takes place. The simulation volume considered for that test is too small to contain a large sample of haloes hosting galaxies with significant AGN activity. Durier & Dalla Vecchia (2012) argued that the larger the energy jump, the larger the violation of energy conservation will be when the time-step limiter is not used. As the energy injection in AGN feedback events is two orders of magnitude larger than for stellar feedback, we expect the masses of galaxies with $M_* \gtrsim 3 \times 10^{10}\mathrm{M}_\odot$ (the mass range where AGN feedback starts to be important) to be reduced, compared to the Ref model, even more than the galaxies for which AGN feedback plays no role. Note that the impact of the time-step limiter is much larger than the differences due to the hydrodynamics solver, but smaller than the effect of doubling/halving the feedback strength.

3.2 The sizes of galaxies

Crain et al. (2015) showed that matching the observed GSMF does in general not lead to a realistic population of galaxies in terms of their mass-size relation and mass build up. Alongside galaxy masses, galaxy sizes were therefore considered in the EAGLE project during the calibration of the parameters of the subgrid model for stellar feedback. Crain et al. (2015) demonstrated that numerical limitations tend to make feedback from star formation less efficient at quenching the galaxies if the feedback occurs in dense regions of the ISM. This would lead to galaxies that are too compact and with a specific star formation rate at low redshift that is lower than observed. As a consequence, they also showed that selecting model parameters that lead to galaxies with sizes in agreement with observational data was necessary to obtain a realistic population of galaxies across cosmic time. Assessing the dependence of the galaxy sizes on the hydrodynamics scheme is, hence, crucial.

In Fig. 3, we show the sizes of the galaxies in both the ANARCHY-SPH and GADGET-SPH simulations. The observational data sets from Shen et al. (2003) (SDSS, grey line and shading) and Baldry et al. (2012) (GAMA, white circles) are shown for comparison. The sizes of the simulated galaxies are computed following McCarthy et al. (2012). We fit a Sérsic profile to the projected, azimuthally-averaged surface density profiles. We then extract the half-mass radius of the galaxy, R_{50}, from this profile when integrated to infinity. To match the observational selection of Shen et al. (2003), we select only galaxies that have a Sérsic index $n_s < 2.5$. We use dashed lines where the (0.2 dex) mass bins contain fewer than 10 objects and dotted lines for galaxies that are represented by fewer than 600 star particles. The 1σ scatter around the mean in the ANARCHY-SPH simulation is shown as the blue shaded region for the mass bins that are both well resolved and well sampled. The GADGET-SPH simulation presents a similar scatter.

Both simulations reproduce the observed galaxy size-mass relation. The simulated galaxies lie within $0.1 - 0.2$ dex of either of the two data sets. As was the case for the GSMF, the galaxy sizes are unaffected by the specific details of the hydrodynamics scheme. This implies that the two hydro schemes have similar energy losses in dense gas regions where feedback takes place. Differences much larger than this can be seen when the subgrid model parameters are varied, even if one requires the GSMF to match observations (Crain et al. 2015). Galaxies with $M_* > 10^{11}\mathrm{M}_\odot$ display small, but not statistically significant, differences with the objects in the GADGET simulation being slightly smaller. This is in agreement with the findings of Naab et al. (2007) who, using GADGET-SPH, produced massive galaxies too compact compared to observations.

When considering the galaxy masses, we found that not using the Durier & Dalla Vecchia (2012) time-step limiter led to an increase of the feedback efficiency, although the magnitude of the effect was small compared to that of doubling the feedback energy. As galaxy sizes were our second diagnostic, we also consider the

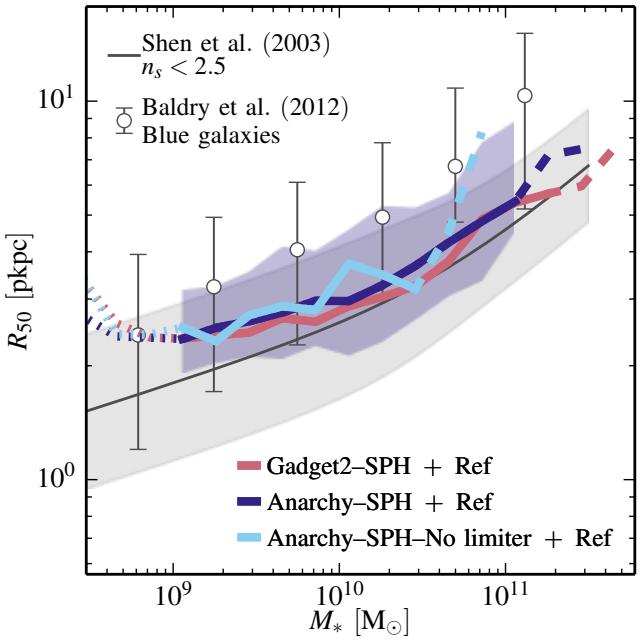

Figure 3. The sizes, at $z = 0.1$, of disc galaxies in the L050N0752 ANARCHY SPH (blue line) and GADGET SPH (red line) simulations and in the ANARCHY SPH model without time-step limiter (cyan line). Size, R_{50}, is defined as the half-mass radius of a Sérsic profile fit to the projected, azimuthally-averaged stellar surface density profile of a galaxy, and those with Sérsic index $n_s < 2.5$ are considered disc galaxies. Curves show the binned median sizes, and are drawn with dotted lines below a mass scale of 600 star particles, and using a dashed line style where sampled by fewer than 10 galaxies per 0.2 dex mass bin. The 1σ scatter about the median of the ANARCHY run is denoted by the blue shaded region. The solid grey line and the grey shading show the median and 1σ scatter of sizes for $n_s < 2.5$ galaxies inferred from SDSS data by Shen et al. (2003), whilst white circles with error bars show sizes of blue galaxies inferred by Baldry et al. (2012) from GAMA data. All simulations reproduce the $z = 0.1$ galaxy sizes.

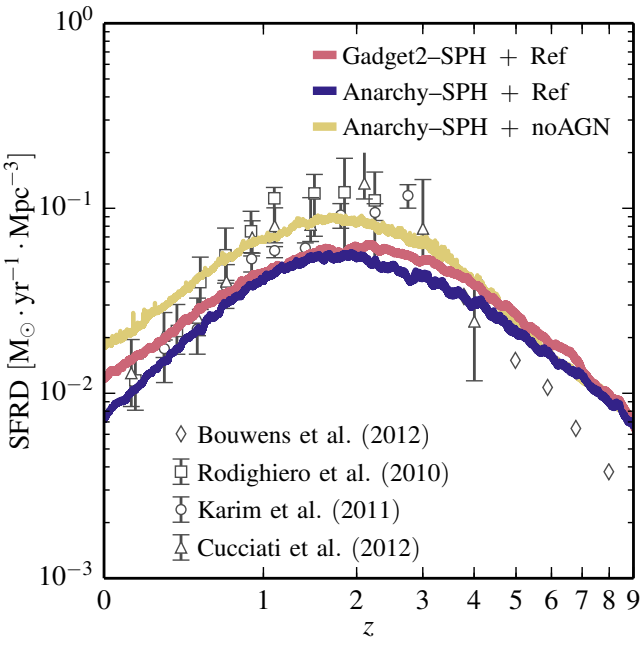

Figure 4. The evolution of the cosmic star formation rate density in both the L050N0752 ANARCHY SPH (blue line) and GADGET-2 SPH (red line) simulations. The data points correspond to observations from Karim et al. (2011) (radio), Rodighiero et al. (2010) (24 μm), Cucciati et al. (2012) (FUV) and Bouwens et al. (2012) (UV). The decline in the star formation rate density from $z = 2$ to $z = 0$ is less pronounced in the GADGET run, leading to a 65% higher star formation rate density at $z = 0$. For comparison, a model without AGN feedback (yellow line) is shown. The star formation rate density in that model has a low-redshift slope similar to that of the GADGET simulation.

effect of switching off this limiter on the sizes of our simulated galaxies. This model is shown as the cyan line in Fig. 3. The oscillations seen in the curve are due to the smaller volume used for this simulation. The sizes of the galaxies are very close to or slightly larger than the ones in the default simulation.

Crain et al. (2015) also showed that using more efficient stellar feedback leads (among other things) to higher SSFRs, lower passive fractions and lower metallicities. We have verified that turning off the time-step limiter has the same qualitative effects, although the differences are small. We will not consider the effect of turning off the limiter further in the rest of this paper.

3.3 The star formation rates of galaxies

We now turn to the star formation rates of galaxies. This quantity was not used in the parameter calibration process of the ANARCHY-SPH run (i.e. the default EAGLE model) and is an important independent diagnostic of the success of the simulation. Furthermore, since the ISM dictates the star formation rates of galaxies, changes in the way the equations of hydrodynamics are solved may lead to changes in the SFRs.

In Fig. 4, we show the average star formation rate per unit volume. The blue and red lines again correspond to the ANARCHY and GADGET flavours of SPH, respectively. Observational data from Rodighiero et al. (2010), Karim et al. (2011), Cucciati et al. (2012) and Bouwens et al. (2012) is also shown. Where applicable, the data has been corrected for our adopted cosmology and IMF as described in Furlong et al. (2015). In agreement with the data, both simulations display a rise in the star formation rate density at high redshifts and a fall at $z \lesssim 2$. As was discussed by Furlong et al. (2015), the constant offset in star formation rate of ≈ 0.2 dex between the simulations and observations leads to 20% less stars being formed over the cosmic history, consistent with the $z = 0.1$ GSMF (Fig. 1), whose "knee" the simulations slightly undershoots.

The simulation using the GADGET version of SPH predicts a higher cosmic star formation rate density than its ANARCHY counterpart between redshifts 2 and 6 but this does not lead to a large difference in stellar mass formed by $z = 2$. However, the higher star formation rate seen at $z < 1$ is important and the smaller decrease between $z = 1$ and $z = 0$ implies a star formation rate that is 65% higher by $z = 0$ in the simulation using the GADGET formulation of SPH. This higher star formation rate can be tentatively related to the larger number of high-mass galaxies seen in the GSMF of this simulation and could, hence, indicate a lower quenching efficiency of the AGN activity in the largest haloes. An extreme version of a model with a low quenching efficiency in large haloes is given by a model without AGN feedback. Such a model, using the ANARCHY flavour of SPH, is shown using the yellow line in Fig. 4. The excess star formation at $z < 2$ is much larger than in the GADGET-SPH based run with AGN feedback, but the slope is similar and not steep enough compared to the data.

Whether the excess star formation rate at low redshift is due

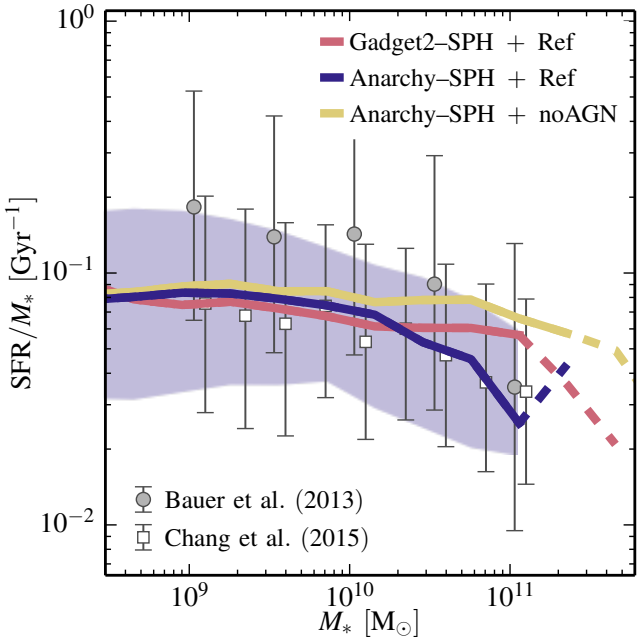

Figure 5. The median specific star formation rate $\dot{M}_*/M_*$, of star-forming galaxies ($\dot{M}_*/M_* > 0.01$ Gyr^{-1}) as a function of stellar mass at $z = 0.1$ in the L050N0752 ANARCHY SPH (blue line) and GADGET-2 SPH (red line) simulations. Dashed line styles are used where the simulation is sampled by fewer than 10 galaxies per 0.2 dex mass bin. The 1σ scatter about the median of the ANARCHY run is denoted by the blue shaded region. Observational data points with error bars correspond to the median and 1σ scatter of the SSFR from GAMA by (Bauer et al. 2013, grey circles) and SDSS+WISE by (Chang et al. 2015, white squares). Galaxies with $M_* > 2 \times 10^{10}$M$_\odot$ have a significantly higher specific star formation rate in the GADGET SPH simulation than in the ANARCHY SPH one, but the decrease is smaller than when AGN activity is turned off (yellow line).

to large haloes can be confirmed by looking at the specific star formation rate (SSFR) of the simulated galaxies. This quantity is shown in Fig. 5 as a function of stellar mass. We limit our selection to star-forming galaxies by excluding objects with $\dot{M}_*/M_* < 0.01$ Gyr^{-1}. As was the case for the stellar mass of the galaxies, we measure the SFR within a 30 kpc spherical aperture. The red and blue lines show the mean SSFR in the simulations using the GADGET and ANARCHY flavours of SPH respectively. As for other figures, the lines are dashed when a given mass bin is sampled by fewer than 10 objects. The blue shaded region indicates the $1-\sigma$ scatter in the ANARCHY-based simulation. The GADGET-based simulation displays a scatter of the same magnitude. For comparison, we show the SSFR inferred from observations in the GAMA survey by Bauer et al. (2013) (grey circles) and observations by Chang et al. (2015) using recalibrated star formation rate indicators based on SDSS+WISE photometry (white squares). Simulated galaxies with masses $M_* \sim 10^{11}$M$_\odot$ are in agreement with the Bauer et al. (2013) data, whilst lower-mass objects exhibit a specific star formation rate lower than observed with the discrepancy reaching ~ 0.3 dex at $M_* \sim 10^9$M$_\odot$. Schaye et al. (2015) showed that part of this discrepancy goes away if the resolution of the simulation is increased. Interestingly, the recalibrated star formation tracers of Chang et al. (2015) lead to lower specific star formation rates in excellent agreement with the EAGLE results. Both the GADGET and ANARCHY simulations show the same behaviour at low masses.

At the upper end of the mass spectrum the two simulations do, however, differ. The star formation rate of galaxies with $M_* \gtrsim 2 \times 10^{10}M_\odot$ is significantly larger for the GADGET formulation of SPH. At $M_* \sim 10^{11}$M$_\odot$, the discrepancy is 0.3 dex.

Complementary to the SSFR of the star forming galaxies, the passive fraction provides a good diagnostic of the efficiency with which SF is quenched in large galaxies This quantity is shown in Fig. 6 for both our simulations. Galaxies are considered passive if their SSFR is smaller than 0.01 Gyr^{-1}, which is an order of magnitude below the observed median SSFR for star forming galaxies at that redshift. For comparison, the data points show the fractions inferred from SDSS data by Gilbank et al. (2010) and Moustakas et al. (2013). We only show points for the simulated population at masses for which there are at least 100 particles at the median SSFR (see Schaye et al. 2015).

The two simulations present a very different behaviour for galaxies with $M_* \gtrsim 2 \times 10^{10}M_\odot$. Whilst the ANARCHY-SPH simulation follows the trend seen in the observational data, the GADGET-SPH simulation shows a constant passive fraction of $\sim 15\%$ at masses up to $M_* = 2 \times 10^{11}$M$_\odot$. At larger masses, the fraction is 0, implying that all galaxies are star-forming, in disagreement with the data that indicates that almost all galaxies ($> 80\%$) of that mass range are passive. Note, however, that there are only 20 galaxies with $M_* > 10^{11}$M$_\odot$ in the simulation volume and that the fractions displayed in Fig. 6 are, hence, affected by small number statistics. Since the ANARCHY and GADGET simulations use the same initial conditions, the comparison between the two schemes is, however, still meaningful. Switching from ANARCHY to standard GADGET has qualitatively a similar effect as switching off AGN feedback (yellow line).

The shortage of passive galaxies in the GADGET simulation at the high-mass end of the galaxy population and the higher SSFR for high-mass objects both indicate that the star formation quenching processes are inefficient in the largest haloes. This higher star formation rate at low redshift in high-mass haloes leads to an increase of the stellar mass of massive galaxies as was hinted at by the difference in the GSMFs between the two simulations at $z = 0.1$ (Fig. 1). AGN feedback, which is the main source of quenching in our model for galaxies with $M_* \gtrsim 2 \cdot 10^{10}M_\odot$, seems to be insufficiently effective at quenching star formation in large haloes in the GADGET simulation.

It is worth mentioning that we cannot eliminate the possibility that a re-calibration of the subgrid parameters could bring the GADGET simulation into agreement with the data. By changing the frequency of the AGN events or the temperature to which the gas is heated during such an event, it might be possible to quench star formation in large galaxies even when the GADGET formulation of SPH is used. It is, however, unclear if this could be achieved and whether subgrid parameters should be used to compensate for the shortcomings of a particular hydro scheme. Similarly, simulations run at different resolutions might lead to different conclusions (if the subgrid parameters are kept fixed). Note that simulations run at a lower resolution (such as the low-redshift versions of OWLS Schaye et al. (2010) and cosmo-OWLS (Le Brun et al. 2014)) have fewer resolution elements in the haloes and may hence not suffer as much from the lack of phase mixing (see discussion below). A full exploration of the subgrid model parameter space or a comprehensive resolution study are, however, beyond the scope of the present paper.

The effectiveness of the AGN feedback can be related to the state of the gas surrounding the galaxies and in the whole halo. The difference can be understood as follows. The accretion of cold gas

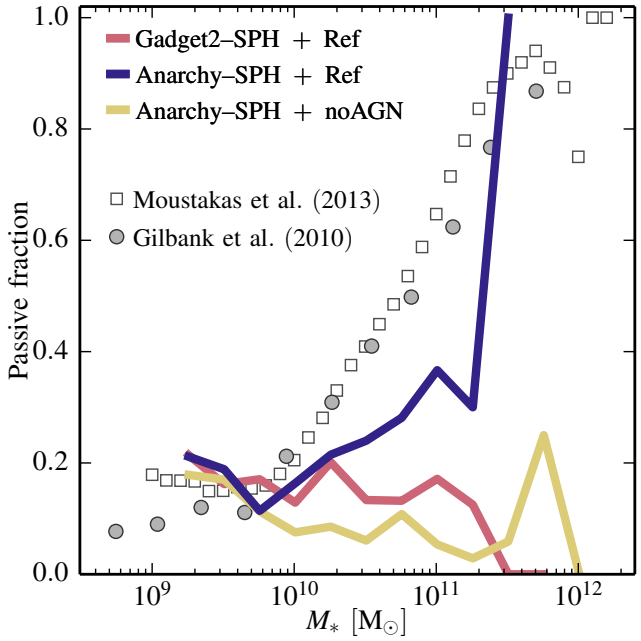

Figure 6. The fraction of passive galaxies ($\dot{M}_*/M_* < 0.01$ Gyr^{-1}) at $z = 0.1$ in both the L050N0752 ANARCHY SPH (blue line) and GADGET SPH (red line) simulations. We only show mass bins that correspond to 100 or more star-forming particles for the median SSFR. The grey circles and white squares correspond to the passive fractions inferred from the SDSS data by Gilbank et al. (2010) and by Moustakas et al. (2013). The passive fraction is far too low for galaxies with $M_* \gtrsim 2\times10^{10}M_\odot$ in the GADGET simulation, in a similar fashion to the ANARCHY simulation without AGN feedback (yellow line).

onto the galaxies from filaments is the key source of fresh material from which stars can be formed in those haloes. The AGN will sustain a hot halo in which these filaments will dissolve. It is likely that the spurious surface tension that plagues the density-entropy formulation of SPH used in GADGET does not leave the gas in the hot halo in a state where the AGN activity can be effective at stopping star formation. An example of these issues would be the inability for dense gas blobs to dissolve in a hot halo medium (see for instance the "blob test" problem by Agertz et al. 2007), which could allow cold pristine gas in filaments to survive the hot bubbles created by the AGN activity and feed the galaxy with gas ready to form stars. The better phase-mixing ability of the ANARCHY formulation of SPH is more effective at disrupting infalling filaments and prevent them from reaching the galaxies, making the AGN-driven bubbles effective at stopping star formation. In this scenario, the issue is not that outflows generated by an AGN are unable to sustain a hot halo (we will show that hot haloes are present in both cases), it is rather the pristine gas that forms clumps that are unstable and cool rather than being mixed in. The next section further explores the differences in gas properties of the two simulations.

4 LARGE- AND SMALL-SCALE GAS DISTRIBUTION

In the previous section, we showed that the masses and sizes of galaxies are only marginally affected by the improvements to the hydrodynamics scheme made in the ANARCHY flavour of SPH. We also showed, however, that the star formation rates of massive galaxies are significantly affected by these same improvements and argued that some of the differences might be directly related to the way in which the different SPH schemes treat the gas in large haloes. In this section, we explore this possibility by studying the state of the gas both outside and inside haloes. We will focus on the largest systems, where the dynamical time is similar to or shorter than the cooling time of the hot gas, and hence the hydrodynamic forces become important.

4.1 Gas in large-scale structures

A simple diagnostic of the state of the gas in a simulation is the distribution of the SPH particles or grid cells in the density-temperature plane. The different components (ISM, IGM, etc.) can then be identified and their relative abundance in terms of mass or volume estimated. Since the ANARCHY and GADGET formulations behave differently when different phases are in contact or in the presence of a shock, it is worth analysing the differences created by those schemes. In order to minimize the impact of the subgrid models on the distribution of the gas, we start by looking at the gas in the inter-halo medium, i.e. the gas outside of haloes. Most of the gas that is located outside of haloes has had little contact with star forming regions or with the winds driven by AGN and star formation but some of the material might have been enriched early on in proto-haloes (e.g. Oppenheimer et al. 2012). We are hence focusing on the low-metallicity, mostly primordial, gas before it falls onto haloes. This should allow us to consider differences driven mostly by the two flavours of the hydrodynamics scheme.

The haloes have been identified using the FoF algorithm and are hence typically larger than the commonly given virial radii. This ensures that we are not considering particles that are part of any resolved haloes. In both our simulations, we only identify haloes that have more than 32 particles, effectively imposing a minimum halo mass of $M_{\rm FoF} = 3.1 \times 10^8M_\odot$. This analysis is resolution dependent via the definition of the minimum halo mass resolved by the simulation. If the resolution were increased, one would find smaller haloes, meaning that some of the particles that we identify as being outside of any halo will become part of small haloes. However, small haloes are unlikely to host large amounts of star formation and drive enrichment and feedback. As both simulations have been run at the same resolution with the same initial conditions, the same objects will collapse and form haloes, ensuring that our one-to-one comparison is not compromised by the potential presence of smaller unresolved structures.

In Fig. 7, we show the distribution of the gas outside of all FoF groups in the density-temperature plane at $z = 0$ for GADGET-SPH (left panel) and ANARCHY-SPH (right panel). The low-density material ($n_{\rm H} < 10^{-4}$ cm^{-3}) is in a very similar state in the two simulations with an extended distribution of diffuse material spanning more than 4 orders in magnitude in temperature. The higher temperature material has been heated by feedback activity and blown out of the haloes in both simulations. Differences start to appear at intermediate densities (10^{-4} cm^{-3} $< n_{\rm H} < 10^{-1}$ cm^{-3}). A lot more mass resides in that regime in the simulation using the GADGET formulation of SPH. Because of the artificial surface tension appearing in GADGET-SPH between different phases in contact discontinuities, this dense gas is unable to properly mix with the lower density, higher temperature material surrounding it. In the ANARCHY simulation, the use of both the Pressure-Entropy formulation of the SPH equations and of a (small numerical) diffusion term has allowed this dense gas to dissolve into its surroundings. The difference is even more striking at higher densities ($n_{\rm H} > 10^{-1}$ cm^{-3}), where no gas is present in the ANARCHY simulation, whilst a sig-

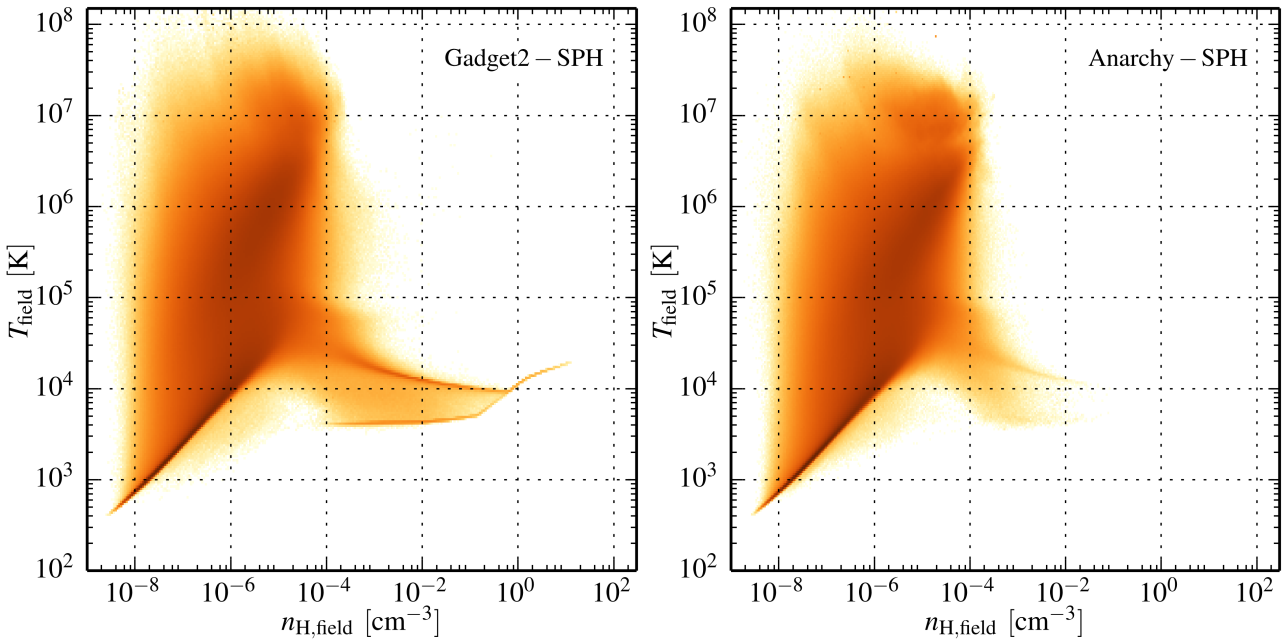

Figure 7. The mass-weighted distribution of gas outside of collapsed structures in the density-temperature plane. The left panel shows the $z = 0$ distribution for the GADGET SPH simulation whereas the right panel shows the equivalent distribution for the ANARCHY SPH simulation. The GADGET SPH run displays high-density gas on the imposed equation of state whilst there is no gas in the ANARCHY SPH run above a density of $n_{\rm H} > 10^{-1}{\rm cm}^{-3}$. Dense star forming gas is mixing with the lower-density, higher-temperature medium in the ANARCHY SPH run, whilst the artificial surface tension introduced by the GADGET SPH formulation prevents this gas from dissolving and leads to star formation outside of haloes.

nificant amount is present in the GADGET one. This difference is especially important since, depending on its metallicity, some of this dense gas may be star-forming. Star formation is hence taking place outside of collapsed structures in the simulation using GADGET. Interestingly, this high-density gas also has a high metallicity ($Z \gtrsim 0.1 Z_{\odot}$). This gas has thus been ejected from haloes after having been enriched by star formation. In ANARCHY-SPH, similar material would likely be dissolved into the surrounding lower-density medium, either outside haloes or in winds inside haloes.

4.2 Extragalactic gas in haloes

We find that within haloes differences in the density-temperature diagram are best quantified by looking at the distribution of star forming gas. We define the IntraGroup Medium (IGrM) as the gas within R_{200} but outside of 30 kpc masks placed at the centre of each subhalo. This excludes the gas present in the ISM or close to galaxies and should leave us with a reasonable definition of the IGrM.

In Fig. 8, we show the star formation rate of the IGrM as a function of the halo mass M_{200} at $z = 0.1$ for objects extracted from the ANARCHY simulation (blue squares) and the GADGET-SPH simulation (red circles). Haloes with masses $M_{200} \gg 10^{12}{\rm M}_{\odot}$ have a higher star formation rate in the IGrM in the simulation using the GADGET formulation of SPH than in the ANARCHY simulation. The higher fraction of dense gas ($n_{\rm H} > 10^{-1}$ cm^{-3}) in the GADGET simulation leads to a higher IGrM star formation rate. The specific star formation of the IGrM corresponds to $\approx 5 \times 10^{-3}$ Gyr^{-1} in the GADGET simulation and is more than an order of magnitude lower ($\approx 4 \times 10^{-4}$ Gyr^{-1}) for ANARCHY. Although these values are low when compared to the typical values for galaxies (see Fig. 5), the presence of significant star formation in the IGrM indicates that the AGN activity or gravitational heating is not effective enough at quenching star formation in the largest haloes.

As the haloes in the GADGET-based simulation exhibit more star formation in their IGrM, it is interesting to investigate how the dense gas is distributed spatially. To this end, we selected the most massive halo ($M_{200} \approx 2 \times 10^{14}{\rm M}_{\odot}$) in both simulations and constructed column density maps of the gas. As we are mainly interested in the dense gas and to increase the clarity of the maps, we only select gas with $n_{\rm H} > 10^{-2}$ cm^{-3}. As discussed above, the behaviour of the warm diffuse medium is similar for both formulations of the SPH equations and can hence be safely discarded here.

These dense gas column density maps are shown in Fig. 9 for the GADGET (left panel) and ANARCHY (right panel) simulations. The large dashed circles indicate the position of the spherical overdensity radius, $R_{200} \approx 1.1$ Mpc, whilst the small solid circles indicate the innermost 100 kpc, where the effects of the central galaxies on the gas will be maximized. We will not consider this central region in the remainder of this subsection since, as was discussed in section 3, in this region the differences due to the hydro solver are likely to be smaller than the ones induced by small variations in the subgrid parameters.

The difference between the two maps is striking. The halo from the GADGET simulation contains a large number of dense clumps of gas at all radii, as was found in the simulations of Kaufmann et al. (2009). These clumps can be seen even inside the inner 100 kpc where feedback from both the AGN and star formation might be expected to disrupt them. These nuggets of dense gas also accompany the in-falling satellites. The map extracted from the ANARCHY simulation is much smoother and dense gas is found mostly in the wakes of in-falling satellite galaxies following their stripping. ANARCHY's ability to mix phases in contact discontinuity allows dense clumps to dissolve into the hot halo, whereas the spurious

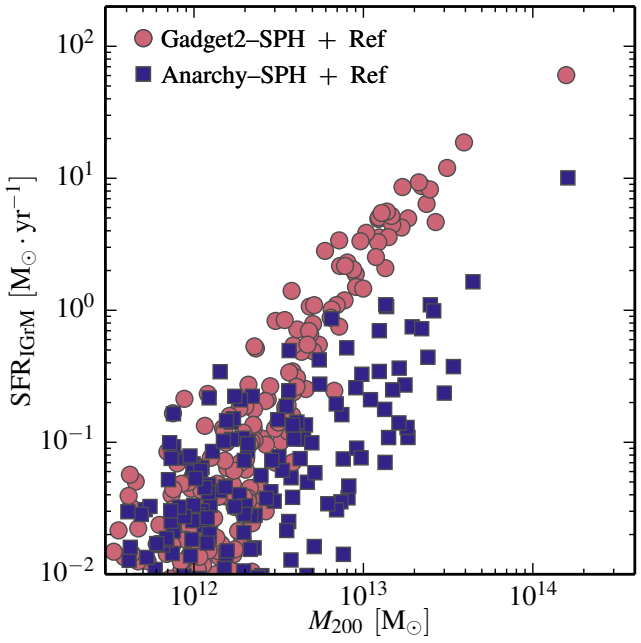

Figure 8. The star formation rate of the inter-group medium (IGrM), i.e. inside the halo but at least 30 kpc from any identified galaxy, as a function of halo mass at $z = 0.1$ for the L050N0752 ANARCHY SPH (blue squares) and GADGET SPH (red circles) simulations. The IGrM is forming significantly more stars in group- and cluster-mass haloes ($M_{200} > 5\times10^{12}\mathrm{M_\odot}$) in the run using the GADGET SPH scheme.

surface tension that appears between phases in GADGET SPH allows them so survive and perhaps even grow. Since some clumps reach densities that exceed the threshold for star formation, some of them will increase the SF rate of the IGrM. Here, the flavour of SPH has a direct consequence on the observables extracted from the simulation.

Another observable that may be affected by the choice of hydrodynamics scheme is the gas fraction. In Fig. 10, we show the result of mock X-ray observations of our haloes. Following the method described in Le Brun et al. (2014), we realise mock X-ray observations of our haloes and, assuming hydrostatic equilibrium, infer the halo mass and gas fraction following the same analysis that is applied to observational data. For comparison, we show data from Vikhlinin et al. (2006), Maughan et al. (2008), Sun et al. (2009), Pratt et al. (2009) and Lin et al. (2012). We only selected clusters at $z < 0.25$. As was discussed by Schaye et al. (2015), the simulation using the ANARCHY flavour of SPH (blue squares), the Ref model of EAGLE, overshoots the extrapolated trend seen for higher-mass haloes. This indicates either that the amount of X-ray gas in these haloes is too high or that the gas is in the wrong thermodynamic state. The analysis of a larger simulation volume with more haloes overlapping with the observations motivated Schaye et al. (2015) to introduce an alternative model (labelled AGNdT9) for which the mock-observation inferred gas fractions are in better agreement with the trend in the data. This model uses more sparse, but also more energetic AGN heating events and is shown in Fig. 10 using yellow triangles[3].

Interestingly, the EAGLE Ref model using the GADGET version of SPH (red circles) yields results that are very similar to the improved AGNdT9 model combined with ANARCHY-SPH. The gas fractions are in reasonable agreement with the data. However, the analysis of the dense gas maps and the following discussion indicates that this better agreement is mostly accidental and not a success of the model. The X-ray inferred gas fractions are driven down by a change in the gas mass in the haloes but also by the presence of cold and dense gas in the IGrM that does not emit X-ray and hence artificially reduces the inferred gas masses. The cold clumps lead to the star formation seen in Fig. 7. We note, however, that these spurious undisrupted clumps of dense gas are unlikely to affect simulations of the IGrM done at lower resolution such as those of McCarthy et al. (2010) or Le Brun et al. (2014). Spurious surface tension, preventing the mixing of phase, only appears when $\mathcal{O}(10)$ particles are part of a cold gas fragment. In lower-resolution simulation such gas blobs are sampled by fewer particles and will mix with their environment.

The significant difference in star formation rates in massive haloes seen between the two formulations of SPH can have consequences for quantities that are directly observable. An example of such an observable is the I-band luminosity of groups and clusters (e.g. Sanderson et al. 2013). For galaxies with similar masses and metallicities (as is the case when comparing matched pairs of galaxies extracted from both our simulations), a higher I-band luminosity indicates a younger population of stars and a higher star formation rate over the last billion years. In Fig. 11, we show the I-band luminosity as a function of halo mass $M_{500,\mathrm{hse}}$. The values are computed by generating mock-observations of our haloes as described by Le Brun et al. (2014). Their procedure allows us to compute the halo mass and radius assuming hydro-static equilibrium as is done in observations of actual clusters. The (Cousin) I-band luminosity is computed within $R_{500,\mathrm{hse}}$, the overdensity radius inferred by assuming hydrostatic equilibrium in the analysis of the mock observations. For comparison, we show observational data taken from Sanderson et al. (2013), Gonzalez et al. (2013) and Kravtsov et al. (2014) as well as the SDSS image stacking result of Budzynski et al. (2014). In all cases we selected only clusters at $z < 0.25$.

As expected from the previous analysis of the star formation rates, we find that the I-band luminosity in the groups and clusters extracted from the simulation using the GADGET flavour of SPH is higher than when using ANARCHY. It is also higher than the trend extrapolated from observational data as expected from our analysis of the specific star formation rates and the passive fractions for massive ($M_* > 10^{11}\mathrm{M_\odot}$) galaxies. In the same figure, we also show the group and cluster luminosities extracted from the simulation using the AGNdT9 model and the ANARCHY SPH scheme. The I-band luminosity as a function of mass for that model is very similar to the one obtained using the Ref model. The differences between the GADGET and ANARCHY based simulations are much larger. However, as discussed earlier, changing the model parameters for feedback from star formation will have an even larger effect.

4.3 ISM and CGM gas

We now turn to the gas inside galaxies or in their direct vicinity. The state of this gas will retain some of the properties of the IGrM but will also be directly affected by the subgrid models.

[3] We note that the map of the column density of dense gas of the largest halo in this model is very similar to the one using the Ref model and the ANARCHY code (Fig. 9, right panel). There is no large pool of dense gas clumps floating in the halo.

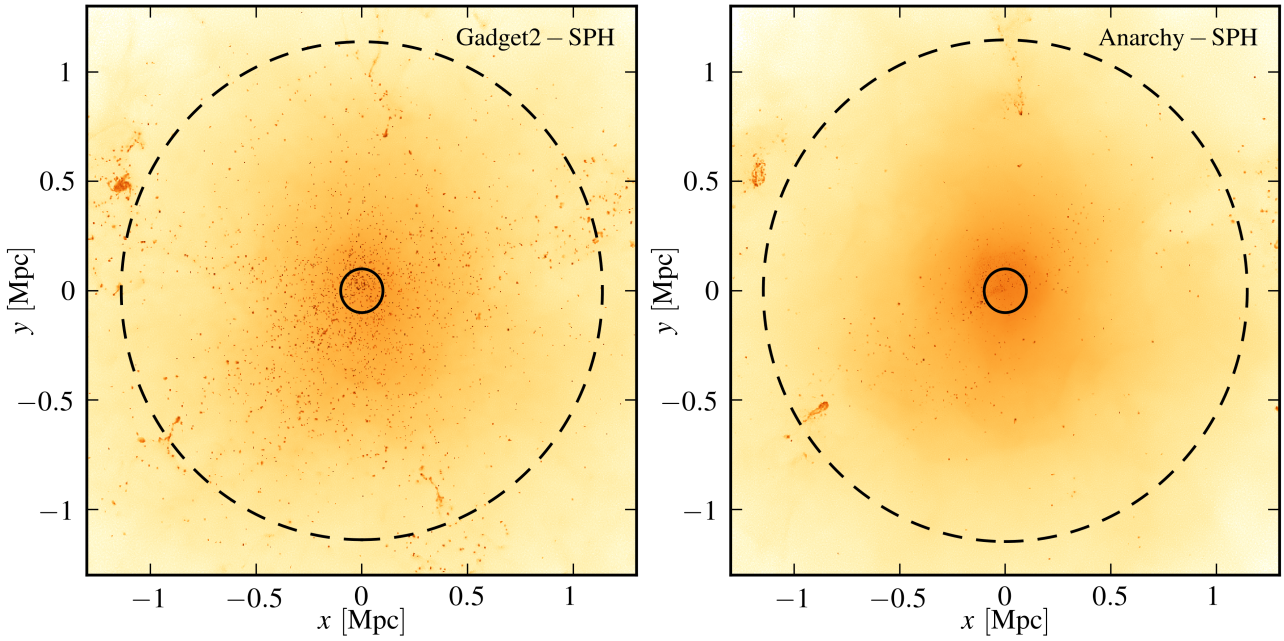

Figure 9. Maps of the column density of dense gas ($n_{\rm H} > 0.01$ cm^{-3}) in the largest haloes ($M_{200} \approx 2 \times 10^{14}M_\odot$) of the L050N0752 GADGET SPH (left panel) and ANARCHY SPH (right panel) simulations. The large dashed circle shows the location of the spherical overdensity radius R_{200}, whilst the small solid circle in the centre encloses the inner 100 kpc. The halo in the GADGET SPH run contains a large number of dense clumps of gas, as was found by Kaufmann et al. (2009) in their simulations, while its counterpart in the ANARCHY SPH run displays a much smoother gas distribution. The spurious surface tension appearing in the GADGET formulation of SPH makes it difficult for the dense gas stripped from the in-falling satellites to be disrupted and mixed into the IGrM.

We first focus on the cold and dense phase of the gas. With the help of careful simulations using radiative transfer, Rahmati et al. (2013) showed that cold ($T < 10^{4.5}$ K) and dense ($n_{\rm H} > 0.01$ cm^{-3}) gas is a good proxy for H I gas. They provide a fitting function to compute H I, but for the purpose of this paper, setting the H I fraction to 1 for all this cold and dense gas is a sufficiently good approximation. In Fig. 12, we show the mass function of the H I gas in the ANARCHY (blue line) and GADGET (red line) simulations. We use dashed lines when the mass bins contain fewer than 10 objects and dotted lines when the H I mass corresponds to fewer than 300 SPH particles. We measured the H I mass using fixed spherical apertures placed at the centre of each subhalo in order to only select the gas in the ISM and circum-galactic medium (CGM). As a point of reference, we show the best-fitting Schechter functions to the data of Haynes et al. (2011) (ALFALFA survey) and Zwaan et al. (2003) (HIPASS survey).

As expected from the non-disruption of cold gas in the hot halo, there is an over-abundance of massive H I objects in the simulation using the GADGET variant of SPH. Whilst the simulation using ANARCHY is in reasonable agreement with the observations, the same model using GADGET overshoots the break in the mass function and vastly over-predicts the abundance of H I clouds of mass $M_{\rm HI} > 10^{10}$ M$_\odot$. Both simulations under-predict the abundance of low-mass ($M_{\rm HI} \lesssim 2 \times 10^9$ M$_\odot$) H I clouds. As is shown by Crain et al. (in prep) for ANARCHY, this is a resolution effect. Simulations run with both flavours of SPH exhibit the same behaviour in that regime and can then likely be rescued in a similar way by increasing the resolution.

The discrepancy at the high-mass end is another sign that the densest gas clumps found in the group- and cluster-like haloes are not disrupted by the hot halo. They also seem to survive AGN activity and the effect of stellar feedback. These large pools of cold gas in massive haloes are not observed and are likely to be responsible for the spurious star formation seen in the largest galaxies (Figs. 5 and 6). We note that it might be possible to modify the AGN subgrid model so as to disrupt those clouds without breaking other constraints imposed on the model. However, it seems unlikely that this purely numerical issue can be completely alleviated. Furthermore, the abundance of spurious cold clumps will increase with the resolution (as larger fluctuations in the density distribution can be sampled), implying that the AGN activity needed to suppress them would also have to be modified.

5 SUMMARY & CONCLUSION

The aim of this study was to investigate the effects of the improved hydrodynamics solver and time stepping used for the EAGLE suite of cosmological simulations (Schaye et al. 2015; Crain et al. 2015). By running the same simulation without re-calibrating the subgrid model parameters with both EAGLE's ANARCHY and the standard GADGET formulations of the SPH equations, we were able to isolate the effects of the hydrodynamics solver. Thanks to the use of the pressure-entropy formulation of SPH (Hopkins 2013), a more stable kernel function (Dehnen & Aly 2012), a small amount of numerical diffusion (Price 2008), an improved viscosity switch (Cullen & Dehnen 2010) and the Durier & Dalla Vecchia (2012) time-step limiter, the ANARCHY flavour of SPH is able to reproduce a large set of hydrodynamical tests more accurately than the GADGET flavour (Dalla Vecchia in prep., Sembolini et al. 2015). Here we investigated whether the better mixing of gas phases implied by these changes, as well as the improved treatment of viscosity in shear flow, have consequences for the simulation of haloes and

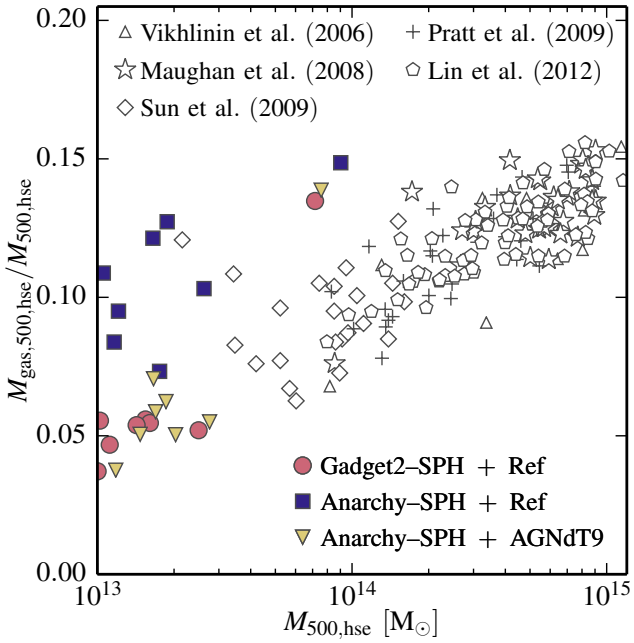

Figure 10. The $z = 0$ gas fractions within $R_{500,\rm hse}$ as a function of $M_{500,\rm hse}$ inferred from virtual X-ray observations of the L050N0752 ANARCHY SPH (blue squares) and GADGET SPH (red circles) simulations. Data points correspond to measurements from Vikhlinin et al. (2006) (triangles), Maughan et al. (2008) (stars), Sun et al. (2009) (diamonds), Pratt et al. (2009) (crosses) and Lin et al. (2012) (pentagons). The ANARCHY SPH Ref model overpredicts the gas fractions for group-sized objects but this can be solved by using the AGNdT9 prescription for AGN feedback (yellow triangles). The haloes of the GADGET SPH run are in better agreement with the data as a result of their higher fraction of cold gas that artificially reduces the X-ray inferred gas fractions.

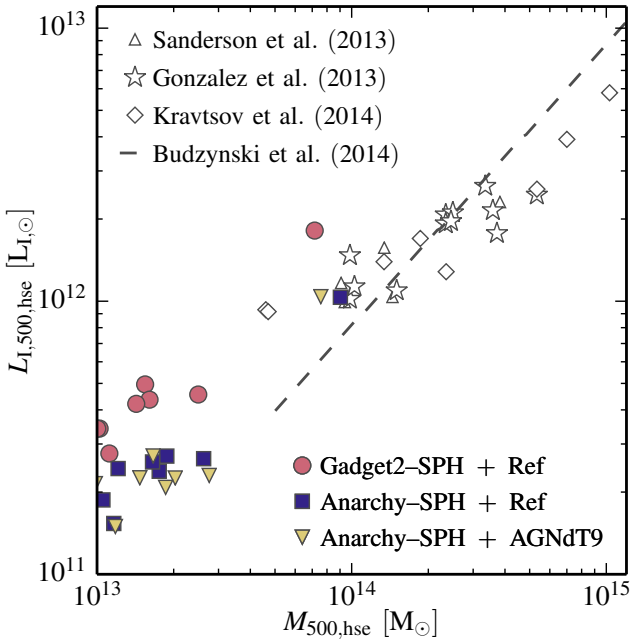

Figure 11. I-Band luminosity within $R_{500,\rm hse}$ as a function of $M_{500,\rm hse}$ at $z = 0$ in the L050N0752 ANARCHY SPH (blue squares) and GADGET SPH (red circles) simulations. The yellow triangles show the haloes extracted from the ANARCHY SPH run with an improved AGN model (AGNdT9).Data points correspond to the observations of Sanderson et al. (2013) (triangles), Gonzalez et al. (2013) (stars), Kravtsov et al. (2014) (diamonds) and the dashed line represents the SDSS image stacking results of Budzynski et al. (2014). Where necessary, observations were converted to the I-band following Le Brun et al. (2014). The GADGET SPH run overestimates the I-band luminosity in the group- and cluster-size objects as expected from the absence of passive galaxies in that simulation (see Fig. 6).

galaxies. Our analysis of the differences can be summarized as follows:

(i) Except for the most massive objects, the masses and sizes of the simulated galaxies are largely unaffected by the choice of SPH flavour. Uncertainties in the subgrid parameters lead to much larger differences (Figs. 1 and 3).

(ii) The absence of the Durier & Dalla Vecchia (2012) time-step limiter leads to somewhat more efficient feedback, as expected from the non-conservation of energy occurring in feedback events when the limiter is neglected. For low-mass galaxies its effect is larger than that of the choice of hydro solver but small compared to the changes in the subgrid models for feedback (Figs. 2 and 3). For AGN feedback the time-step limiter might have a similar or stronger effect since the energy per feedback event is greater than for stellar feedback.

(iii) The star formation rates of galaxies in small haloes, where the cooling time is smaller than the dynamical time, are unaffected by the change of hydrodynamics scheme. However, in massive haloes the star formation rates are much higher in the simulation using GADGET SPH (Figs. 5, 6 and 11). These differences in behaviour can be related to the lower quenching power of the AGN activity in that simulation. The lack of phase mixing, coming from the spurious artificial surface tension appearing at contact discontinuities, prevents cold dense gas from dissolving into the hot halo (Figs. 7 and 9).

(iv) This cold dense gas then reaches the central galaxies and leads to increased star formation (Figs. 5 and 6) in both the central galaxies and intragroup medium (Fig. 8). This also leads to a lower hot gas fraction in the haloes (Fig. 10) and an oversestimate of the H I mass (Fig. 12).

Our results indicate that the improved hydrodynamics scheme plays a significant role in hot hydrostatic gas haloes, but not for lower-mass galaxies. Our results are resolution dependent and it is possible that simulations performed at much higher resolution will be more sensitive to the accuracy of the hydrodynamics solver. Finally, we also stress that some of the differences between the simulations could potentially be cancelled by changing the values of some of the subgrid parameters.

ACKNOWLEDGEMENTS

We thank the anonymous referee for their help improving this paper. This work would have not be possible without Lydia Heck and Peter Draper's technical support and expertise. This work was supported by the Science and Technology Facilities Council (grant number ST/F001166/1); European Research Council (grant numbers GA 267291 "Cosmiway" and GA 278594 "GasAroundGalaxies") and by the Interuniversity Attraction Poles Programme initiated by the Belgian Science Policy Office (AP P7/08 CHARM).

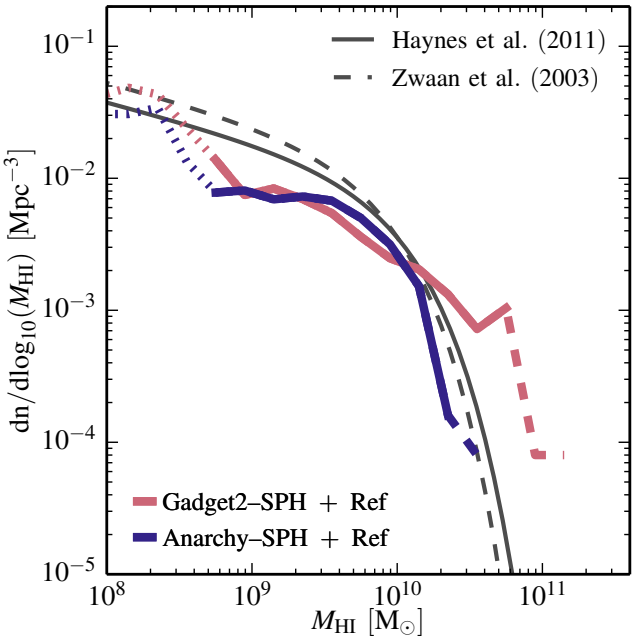

Figure 12. The mass function of H I-like gas (gas with $n_{\mathrm{H}} > 0.01\ \mathrm{cm}^{-3}$, $\mathrm{T} < 10^{4.5}$ K) in the L050N0752 ANARCHY SPH (blue line) and GADGET SPH (red line) simulations. Curves are drawn with dotted lines below a mass scale of 300 star particles, and with a dashed line style where sampled by fewer than 10 galaxies per 0.2 dex mass bin. The solid and dashed grey lines show the best-fitting Schechter fits to the ALFALFA data by Haynes et al. (2011) and HIPASS data by Zwaan et al. (2003), respectively. The simulation using the GADGET SPH formulation strongly overestimates the abundance of massive H I clouds.

This work used the DiRAC Data Centric system at Durham University, operated by the Institute for Computational Cosmology on behalf of the STFC DiRAC HPC Facility (www.dirac.ac.uk). This equipment was funded by BIS National E-infrastructure capital grant ST/K00042X/1, STFC capital grant ST/H008519/1, and STFC DiRAC Operations grant ST/K003267/1 and Durham University. DiRAC is part of the National E-Infrastructure. We acknowledge PRACE for awarding us access to the Curie machine based in France at TGCC, CEA, Bruyères-le-Châtel. RAC is a Royal Society University Research Fellow.

REFERENCES

Abel T., 2011, MNRAS, 413, 271
Agertz O., et al., 2007, MNRAS, 380, 963
Baldry I. K., et al., 2012, MNRAS, 421, 621
Balsara D. S., 1995, Journal of Computational Physics, 121, 357
Bauer A. E., et al., 2013, MNRAS, 434, 209
Beck A. M., et al., 2015, preprint, (arXiv:1502.07358)
Behroozi P. S., Wechsler R. H., Conroy C., 2013, ApJ, 770, 57
Booth C. M., Schaye J., 2009, MNRAS, 398, 53
Bouwens R. J., et al., 2012, ApJ, 754, 83
Budzynski J. M., Koposov S. E., McCarthy I. G., Belokurov V., 2014, MNRAS, 437, 1362
Chabrier G., 2003, PASP, 115, 763
Chang Y.-Y., van der Wel A., da Cunha E., Rix H.-W., 2015, ApJS, 219, 8
Crain R. A., et al., 2015, MNRAS, 450, 1937
Cucciati O., et al., 2012, A&A, 539, A31
Cullen L., Dehnen W., 2010, MNRAS, 408, 669
Dalla Vecchia C., Schaye J., 2012, MNRAS, 426, 140
Davis M., Efstathiou G., Frenk C. S., White S. D. M., 1985, ApJ, 292, 371
Dehnen W., Aly H., 2012, MNRAS, 425, 1068
Dolag K., Borgani S., Murante G., Springel V., 2009, MNRAS, 399, 497
Durier F., Dalla Vecchia C., 2012, MNRAS, 419, 465
Frenk C. S., et al., 1999, ApJ, 525, 554
Furlong M., et al., 2015, MNRAS, 450, 4486
Gilbank D. G., Baldry I. K., Balogh M. L., Glazebrook K., Bower R. G., 2010, MNRAS, 405, 2594
Gingold R. A., Monaghan J. J., 1977, MNRAS, 181, 375
Gonzalez A. H., Sivanandam S., Zabludoff A. I., Zaritsky D., 2013, ApJ, 778, 14
Haardt F., Madau P., 2001, in Neumann D. M., Tran J. T. V., eds, Clusters of Galaxies and the High Redshift Universe Observed in X-rays. (arXiv:astro-ph/0106018)
Haas M. R., Schaye J., Booth C. M., Dalla Vecchia C., Springel V., Theuns T., Wiersma R. P. C., 2013, MNRAS, 435, 2931
Haynes M. P., et al., 2011, AJ, 142, 170
Hopkins P. F., 2013, MNRAS, 428, 2840
Hopkins P. F., 2015, MNRAS, 450, 53
Hu C.-Y., Naab T., Walch S., Moster B. P., Oser L., 2014, MNRAS, 443, 1173
Karim A., et al., 2011, ApJ, 730, 61
Kaufmann T., Bullock J. S., Maller A. H., Fang T., Wadsley J., 2009, MNRAS, 396, 191
Kereš D., Vogelsberger M., Sijacki D., Springel V., Hernquist L., 2012, MNRAS, 425, 2027
Kravtsov A., Vikhlinin A., Meshscheryakov A., 2014, preprint, (arXiv:1401.7329)
Lagos C. d. P., et al., 2015, MNRAS, 452, 3815
Le Brun A. M. C., McCarthy I. G., Schaye J., Ponman T. J., 2014, MNRAS, 441, 1270
Li C., White S. D. M., 2009, MNRAS, 398, 2177
Lin Y.-T., Stanford S. A., Eisenhardt P. R. M., Vikhlinin A., Maughan B. J., Kravtsov A., 2012, ApJ, 745, L3
Lucy L. B., 1977, AJ, 82, 1013
Marri S., White S. D. M., 2003, MNRAS, 345, 561
Maughan B. J., Jones C., Forman W., Van Speybroeck L., 2008, ApJS, 174, 117
McCarthy I. G., et al., 2010, MNRAS, 406, 822
McCarthy I. G., Schaye J., Font A. S., Theuns T., Frenk C. S., Crain R. A., Dalla Vecchia C., 2012, MNRAS, 427, 379
Mitchell N. L., McCarthy I. G., Bower R. G., Theuns T., Crain R. A., 2009, MNRAS, 395, 180
Monaghan J. J., 1997, Journal of Computational Physics, 136, 298
Morris J. P., Monaghan J. J., 1997, Journal of Computational Physics, 136, 41
Moster B. P., Naab T., White S. D. M., 2013, MNRAS, 428, 3121
Moustakas J., et al., 2013, ApJ, 767, 50
Naab T., Johansson P. H., Ostriker J. P., Efstathiou G., 2007, ApJ, 658, 710
O'Shea B. W., Nagamine K., Springel V., Hernquist L., Norman M. L., 2005, ApJS, 160, 1
Okamoto T., Jenkins A., Eke V. R., Quilis V., Frenk C. S., 2003, MNRAS, 345, 429
Oppenheimer B. D., Davé R., Katz N., Kollmeier J. A., Weinberg D. H., 2012, MNRAS, 420, 829
Planck Collaboration et al., 2014, A&A, 571, A16
Portinari L., Chiosi C., Bressan A., 1998, AAP, 334, 505
Pratt G. W., Croston J. H., Arnaud M., Böhringer H., 2009, A&A, 498, 361
Price D. J., 2004, PhD thesis, Institute of Astronomy, Madingley Rd, Cambridge, CB2 0HA, UK
Price D. J., 2008, Journal of Computational Physics, 227, 10040
Price D. J., 2012, Journal of Computational Physics, 231, 759
Rahmati A., Pawlik A. H., Raičevič M., Schaye J., 2013, MNRAS, 430, 2427
Rahmati A., Schaye J., Bower R. G., Crain R. A., Furlong M., Schaller M., Theuns T., 2015, MNRAS, 452, 2034
Read J. I., Hayfield T., Agertz O., 2010, MNRAS, 405, 1513

Ritchie B. W., Thomas P. A., 2001, MNRAS, 323, 743
Rodighiero G., et al., 2010, A&A, 518, L25
Rosas-Guevara Y. M., et al., 2013, preprint, (arXiv:1312.0598)
Rosswog S., Davies M. B., Thielemann F.-K., Piran T., 2000, A&A, 360, 171
Saitoh T. R., Makino J., 2009, ApJ, 697, L99
Saitoh T. R., Makino J., 2013, ApJ, 768, 44
Sanderson A. J. R., O'Sullivan E., Ponman T. J., Gonzalez A. H., Sivanandam S., Zabludoff A. I., Zaritsky D., 2013, MNRAS, 429, 3288
Scannapieco C., et al., 2012, MNRAS, 423, 1726
Schaller M., et al., 2015, MNRAS, 451, 1247
Schaye J., 2004, ApJ, 609, 667
Schaye J., Dalla Vecchia C., 2008, MNRAS, 383, 1210
Schaye J., et al., 2010, MNRAS, 402, 1536
Schaye J., et al., 2015, MNRAS, 446, 521
Sembolini F., et al., 2015, preprint, (arXiv:1503.06065)
Shen S., Mo H. J., White S. D. M., Blanton M. R., Kauffmann G., Voges W., Brinkmann J., Csabai I., 2003, MNRAS, 343, 978
Sijacki D., Vogelsberger M., Kereš D., Springel V., Hernquist L., 2012, MNRAS, 424, 2999
Springel V., 2005, MNRAS, 364, 1105
Springel V., 2010a, ARA&A, 48, 391
Springel V., 2010b, MNRAS, 401, 791
Springel V., Hernquist L., 2002, MNRAS, 333, 649
Springel V., White S. D. M., Tormen G., Kauffmann G., 2001, MNRAS, 328, 726
Sun M., Voit G. M., Donahue M., Jones C., Forman W., Vikhlinin A., 2009, ApJ, 693, 1142
Trayford J. W., et al., 2015, MNRAS, 452, 2879
Vikhlinin A., Kravtsov A., Forman W., Jones C., Markevitch M., Murray S. S., Van Speybroeck L., 2006, ApJ, 640, 691
Vogelsberger M., Genel S., Sijacki D., Torrey P., Springel V., Hernquist L., 2013, MNRAS, 436, 3031
Vogelsberger M., et al., 2014, MNRAS, 444, 1518
Wadsley J. W., Veeravalli G., Couchman H. M. P., 2008, MNRAS, 387, 427
Wendland H., 1995, Advances in Computational Mathematics, 4, 389
Wetzstein M., Nelson A. F., Naab T., Burkert A., 2009, ApJS, 184, 298
Wiersma R. P. C., Schaye J., Smith B. D., 2009a, MNRAS, 393, 99
Wiersma R. P. C., Schaye J., Theuns T., Dalla Vecchia C., Tornatore L., 2009b, MNRAS, 399, 574
Zwaan M. A., et al., 2003, AJ, 125, 2842